

# Heterogeneous Integration for Mid-infrared Silicon Photonics

Alexander Spott, *Graduate Student Member, IEEE*, Eric J. Stanton, *Graduate Student Member, IEEE*, Nicolas Volet, Jonathan D. Peters, Jerry R. Meyer, *Fellow, IEEE*, and John E. Bowers, *Fellow, IEEE*

(Invited Paper)

**Abstract**—Heterogeneous integration enables the construction of silicon (Si) photonic systems, which are fully integrated with a range of passive and active elements including lasers and detectors. Numerous advancements in recent years have shown that heterogeneous Si platforms can be extended beyond near-infrared telecommunication wavelengths to the mid-infrared (MIR) (2–20  $\mu\text{m}$ ) regime. These wavelengths hold potential for an extensive range of sensing applications and the necessary components for fully integrated heterogeneous MIR Si photonic technologies have now been demonstrated. However, due to the broad wavelength range and the diverse assortment of MIR technologies, the optimal platform for each specific application is unclear. Here, we overview Si photonic waveguide platforms and lasers at the MIR, including quantum cascade lasers on Si. We also discuss progress toward building an integrated multispectral source, which can be constructed by wavelength beam combining the outputs from multiple lasers with arrayed waveguide gratings and duplexing adiabatic couplers.

**Index Terms**—Silicon photonics, semiconductor lasers, quantum cascade lasers, photonic integrated circuits.

## I. INTRODUCTION

THE vast majority of research on silicon (Si) photonics has focused on devices operating within the near-infrared (NIR) telecommunication bands near 1310 nm and 1550 nm wavelengths. This has been driven chiefly by the prospect of low-cost photonics fabricated with existing complementary metal-oxide-semiconductor (CMOS) infrastructure and the large market for telecommunications with ever increasing demands. While alternative applications of Si photonics and the benefits of integrating optical devices which function at wavelengths outside the telecommunications bands have not been

overlooked, additional challenges have faced the development of longer-wavelength devices.

The mid-infrared (MIR) spectrum, typically defined from 2  $\mu\text{m}$  to 20  $\mu\text{m}$ , demands great interest primarily for gas sensing, defense, and medical applications. Strong and wavelength-selective interactions of light in this regime with many chemicals [1] can be exploited to distinguish substances with multiple spectroscopic techniques. Standoff detection systems, which operate within the MIR transparency windows, can allow remote identification of hazardous materials.

Technologies that address these applications can be miniaturized with chip-scale photonic integration. Si promises a platform for integration solutions at minimal cost due to the existing infrastructure, low material costs, and inherent compatibility with integrated Si electronics systems. It also offers physical advantages compared to other nanophotonic integration material platforms, such as indium phosphide (InP), gallium arsenide (GaAs), or chalcogenide glasses [2]. A high index contrast between Si and deposition-compatible dielectric materials such as silicon nitride ( $\text{Si}_3\text{N}_4$ ) or silicon dioxide ( $\text{SiO}_2$ ) allows light to be well confined within the Si core, enabling exceptionally small devices. The low optical absorption of Si permits extremely high- $Q$  cavities [3], enhancing the sensitivity of integrated sensors. As discussed in this manuscript, it is possible to construct an extremely broadband platform on a Si substrate, which maintains these advantages for waveguides operating from the NIR to the MIR.

The primary challenge for realizing a fully integrated Si photonic platform is to make an efficient light source. Si has an indirect bandgap and corresponding low emission efficiency, which has limited the progress of using Si to generate light. By wafer bonding III-V materials onto processed Si waveguides, heterogeneously integrated III-V/Si devices can be manufactured [4]. This approach allows III-V devices to be constructed on Si with lithographically-limited alignment to Si waveguides. Epitaxial (epi) layer stacks from different III-V growths can be bonded to different areas of a Si chip, allowing a single system to include the III-V materials best suited for each device. This multiple die bonding has been used, for example, to build an integrated triplexer which combines three III-V lasers (operating at 1.31  $\mu\text{m}$ , 1.49  $\mu\text{m}$ , and 1.55  $\mu\text{m}$ ) [5]. The development of Si photonic and heterogeneous integration technologies has progressed rapidly in recent years and photonic integrated circuits

Manuscript received February 16, 2017; revised April 16, 2017; accepted April 17, 2017. This work was supported in part by the Air Force Research Laboratory under Grant BS123456 and in part by the Office of Naval Research under Grant N00014-13-C-0147. The work of N. Volet was supported by the Swiss National Science Foundation. (Corresponding author: Alexander Spott.)

A. Spott, E. J. Stanton, N. Volet, J. D. Peters, and J. E. Bowers are with the University of California, Santa Barbara, Santa Barbara, CA 93106 USA (e-mail: spott@ece.ucsb.edu; estanton@ece.ucsb.edu; volet@ece.ucsb.edu; peters@ece.ucsb.edu; bowers@ece.ucsb.edu).

J. R. Meyer is with the Naval Research Laboratory, Washington, DC 20375 USA (e-mail: jerry.meyer@nrl.navy.mil).

Color versions of one or more of the figures in this paper are available online at <http://ieeexplore.ieee.org>.

Digital Object Identifier 10.1109/JSTQE.2017.2697723

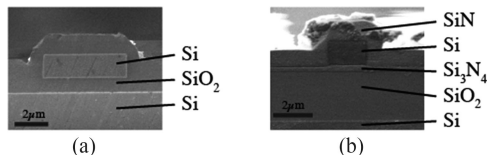


Fig. 1. Scanning electron microscope (SEM) cross sections of (a) SOI and (b) SONOI waveguides with 1.5- $\mu\text{m}$  thick Si waveguides for MIR operation.

(PICs) have now been demonstrated with up to 426 passive and active elements for the NIR [6].

Few PICs have been constructed for operation in the MIR [7], [8], however, although numerous individual passive and active devices for the MIR have been successfully integrated on Si by extending NIR device designs to longer wavelengths. Heterogeneous integration has enabled detectors up to 3.8  $\mu\text{m}$  [7], [9] and, as overviewed here, lasers up to 4.8  $\mu\text{m}$ . All the necessary components for fully integrated MIR Si photonic systems have now been demonstrated.

## II. ARCHITECTURE AND MATERIAL SYSTEMS

Si, SiO<sub>2</sub>, and Si<sub>3</sub>N<sub>4</sub> have low optical material losses in the NIR, allowing Si waveguides with propagation losses below 1 dB/cm [10] and Si<sub>3</sub>N<sub>4</sub> waveguides with ultralow losses below 0.1 dB/m [11]. This, along with the high index contrast afforded by Si-on-insulator (SOI) waveguides, is extremely convenient given the wide availability and high quality of SOI wafers.

However, the material absorption of Si and SiO<sub>2</sub> limits the wavelength range of SOI waveguides. On the shorter-wavelength side of its transparency, the Si absorption begins increasing at  $\lambda \approx 1.2 \mu\text{m}$ . While at longer wavelengths Si continues to transmit light up to  $\lambda \approx 6.8 \mu\text{m}$ , absorption in the SiO<sub>2</sub> begins to increase dramatically for wavelengths longer than  $\sim 3.5 \mu\text{m}$ . Ultimately, the practical wavelength compatibility of SOI waveguides depends on the required transmission losses and the waveguide geometry, which dictate the proportion of light guided within each material.

For relatively large waveguide dimensions, it is still possible to fabricate MIR SOI waveguides with propagation losses smaller than  $\sim 5 \text{ dB/cm}$ . A cross-section scanning electron micrograph (SEM) of a 1.5- $\mu\text{m}$  tall SOI waveguide is shown in Fig. 1(a). Fig. 2 shows preliminary cutback measurements of 2.0- $\mu\text{m}$  wide waveguides measured at  $\lambda \approx 4.8 \mu\text{m}$ . The experimental setup is schematized in Fig. 2(a). An interband cascade laser (ICL) emits MIR light, which is collimated by a Si lens. This free-space beam passes through a quarter-wave plate (QWP) and a half-wave plate (HWP), which are rotated to align the on-chip polarization to either transverse electric (TE) or transverse magnetic (TM). A parabolic mirror (Thorlabs RC02APC) couples the light into a fiber (Thorlabs P3-32F), which is aligned to the input facet with a 3-axis flexure stage (Thorlabs MAX312D) and similarly collected at the output facet. Transmitted power is measured with a photodetector (Boston Electronics PVI-4TE-5) aligned to the output of the collection fiber.

The transmission of waveguides both with and without a plasma-enhanced chemical vapor deposition (PECVD) SiO<sub>2</sub> upper cladding are used to extract the loss. Fig. 2(b) shows

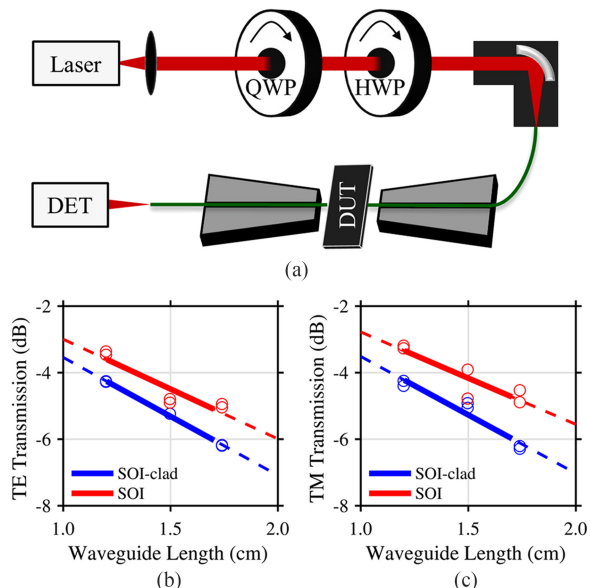


Fig. 2. (a) Schematic of the experimental setup for MIR waveguide loss measurement. Normalized transmission for multiple waveguide lengths are shown for (b) TE polarization and (c) TM polarization.

the measurements for TE-polarized light, which yield losses of  $3.54 \pm 0.11 \text{ dB/cm}$  with cladding and  $3.00 \pm 0.69 \text{ dB/cm}$  without cladding. Fig. 2(c) shows the corresponding measurements for TM polarized light, for which the losses are  $3.51 \pm 0.51 \text{ dB/cm}$  with cladding and  $2.78 \pm 0.79 \text{ dB/cm}$  without cladding. While this is a promising indication that SOI waveguides are suitable for some applications at wavelengths close to 5  $\mu\text{m}$ , these propagation losses will limit the performance of integrated MIR lasers. Furthermore, applications such as *in situ* detection may require MIR waveguides which have lower confinement in the Si core and subsequently increased interaction with the buried SiO<sub>2</sub> layer. Other measurements have shown SOI waveguides with propagation losses below 1 dB/cm at 3.39- $\mu\text{m}$  wavelengths [12].

Alternative material systems can be considered to construct a Si photonics platform for longer wavelengths. A number of waveguide schemes have previously been suggested [13] and demonstrated, including Si-on-sapphire (SOS) [14], germanium-on-Si (GOS) [15]–[17], germanium-on-Si<sub>3</sub>N<sub>4</sub> (GON) [18], Si-on-Si<sub>3</sub>N<sub>4</sub> (SON) [19], suspended Si [20], and chalcogenide-on-Si [21], [22]. These platforms are each suitable for different wavelength ranges and offer other advantages and disadvantages. The ultimate waveguide propagation loss limits are still being explored, with most reported loss values between 1–5 dB/cm. Because sidewall and surface roughness loss are proportional to  $1/\lambda^4$ , losses below 1 dB/cm should be easily achievable in MIR waveguides if material absorption is not the limiting factor.

Among these platforms, one of the more straightforward waveguide schemes is to replace the lower SiO<sub>2</sub> cladding of SOI waveguides with Si<sub>3</sub>N<sub>4</sub> and construct SON waveguides. Si<sub>3</sub>N<sub>4</sub> is easily deposited by PECVD and low pressure chemical vapor deposition (LPCVD) processes, which are CMOS compatible and commonly used in existing Si photonic systems.

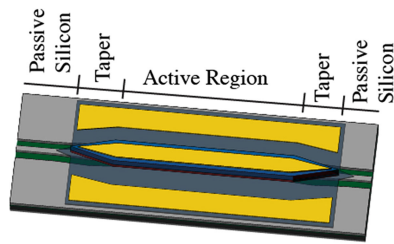


Fig. 3. Three-dimensional schematic of a gain element above a Si waveguide as part of a heterogeneously integrated laser. The III-V layers taper at both ends of the mesa to efficiently transfer light from the hybrid III-V/Si active region to passive Si waveguides. Polished facets or integrated reflectors such as DBR mirrors can form a laser cavity.

These waveguides should maintain low propagation losses at wavelengths from  $\sim 1.2 \mu\text{m}$  to  $\sim 6.7 \mu\text{m}$ .

If a broader wavelength range is desired, a platform can be constructed with multiple waveguiding layers [23], which operate within different spectral limits. For shorter wavelengths where Si absorption is limiting,  $\text{Si}_3\text{N}_4$ -on- $\text{SiO}_2$  waveguides have previously been used [11] and should be suitable for wavelengths from 350 nm to  $3.5 \mu\text{m}$ . The Si-on-nitride-on-insulator (SONOI) platform, as shown in Fig. 1(b), can be constructed by including an additional  $\text{SiO}_2$  layer underneath the  $\text{Si}_3\text{N}_4$  layer of a SON waveguide. This allows the use of both Si-on- $\text{Si}_3\text{N}_4$  waveguides for longer wavelengths and, by etching the top Si layer,  $\text{Si}_3\text{N}_4$ -on- $\text{SiO}_2$  waveguides for shorter wavelengths.

### III. INTEGRATED LIGHT SOURCES

Active elements can be heterogeneously integrated using any of these material systems by bonding III-V materials above the passive device layer after waveguide processing. Light sources have been integrated with Si waveguides for wavelengths from  $1.3 \mu\text{m}$  [24] to  $4.8 \mu\text{m}$  and detectors for wavelengths up to  $3.8 \mu\text{m}$ . Active regions not in a cavity can also be integrated to provide semiconductor optical amplifiers (SOAs) above Si waveguides.

The results and designs discussed here are achieved with low temperature hydrophilic bonding of InP to Si, where an oxygen plasma activation is applied to the surfaces of both materials followed by a  $300^\circ\text{C}$  anneal for about 1 h [25]. Other results use a thin DVS-BCB interlayer between materials. BCB absorption is low at wavelengths up to  $3\text{-}\mu\text{m}$  [26], but may increase the internal device loss for longer wavelengths.

Fig. 3 shows a generalized schematic of a heterogeneously integrated laser source. Here, a III-V mesa sits above a Si waveguide to form a hybrid III-V/Si active region. The III-V mesa is tapered on both sides to transfer light from the hybrid active region to passive Si waveguides on both ends. Tapering schemes can be designed with simultaneous tapering of the Si waveguide to optimize the mode coupling efficiency.

Fig. 4 shows cross-sectional schematics for three possible hybrid III-V/Si active region configurations. In all designs, a fundamental optical mode shares confinement with both the III-V layers and the Si waveguide. The Si waveguide can be either partially etched or fully etched. Both photons and electrical carriers should be confined within the active region to maximize the overlap of the optical mode with the carrier distribution. The

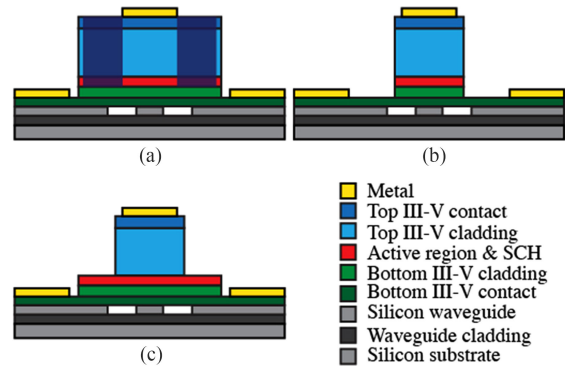


Fig. 4. Active region design options for heterogeneously integrated lasers. (a) A wide III-V mesa above a narrow Si waveguide. Dark areas represent high resistivity regions formed by proton implantation on both sides of a central current channel. (b) A narrow III-V mesa above a narrow Si waveguide. (c) A narrow III-V upper cladding with a wide III-V lower cladding and active region. Alternatively, the narrow upper cladding can be only partially etched.

most common design, shown in Fig. 4(a), includes a very wide (typically near  $24 \mu\text{m}$ ) III-V mesa which sits above a narrow Si waveguide. The optical mode is laterally confined primarily by the width of the Si waveguide, while proton implantation is implemented to form high resistivity regions which confine carriers within a narrow central current channel above the Si waveguide. A careful selection of the Si waveguide and current channel widths is required to ensure single mode operation and optimally overlap the fundamental optical mode with the injected carrier distribution in order to maximize gain and minimize losses. The potential for lasing in parasitic higher-order modes is mitigated as these modes tend to spread laterally, reducing the interaction with the active region in the current channel.

In Fig. 4(b), a narrow III-V mesa laterally confines both the current channel and the optical mode. This design more closely resembles a traditional narrow ridge laser on a native substrate, and is more suitable for lasers with upper cladding materials which are incompatible with proton implantation. A sufficiently narrow III-V mesa is required to completely cut off higher order modes, which can be difficult to achieve at shorter wavelengths. It also increases the interaction of the desired fundamental mode with the mesa sidewalls, potentially adding sidewall roughness-induced internal loss. It is possible to achieve a higher optical confinement factor with this design compared to lasers with wide III-V mesas.

Finally, the design shown in Fig. 4(c) combines a narrow upper cladding with a wide active region. In this design a current channel is defined without proton implantation, but higher order modes still spread laterally as with the proton implanted designs. The active region and SCH layers must therefore be sufficiently thick or the narrow upper cladding should only be partially etched. This scheme has been employed for integrated quantum cascade lasers (QCLs) reviewed here, with a  $1510\text{-nm}$  thick active core.

Heterogeneously integrated lasers with an interlayer such as BCB or  $\text{SiO}_2$  have also been constructed with no Si waveguide within the active region.

A recent in-depth review of NIR heterogeneously integrated lasers and amplifiers can be found in [27].

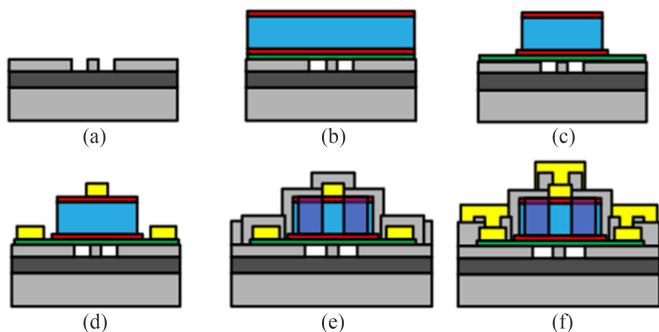


Fig. 5. Generalized process flow of a heterogeneously integrated III-V element with a Si waveguide. (a) Si processing including waveguide and grating etching. (b) Bond III-V layers and remove substrate. (c) Etch III-V mesa, stopping within bottom contact layers. (d) Deposit metal for bottom and top electrodes. (e) Optional: proton implantation to define a current channel. (f) Etch vias and deposit probe metal.

Fig. 5 shows a generalized process flow for an integrated III-V gain material above Si waveguides. Active layers grown on InP, GaAs, and gallium antimonide (GaSb) substrates have been successfully bonded to Si with high yield, although the annealing and substrate removal processes differ in each case.

To facilitate a short taper transition and improve coupling of the Si waveguide mode with the III-V active region, it is necessary that the lower III-V cladding and contact layers are thin. One of the primary fabrication challenges facing the heterogeneous integration of electrically-pumped active elements is etching the III-V mesa precisely down to the bottom-contact layer to deposit metal. The etch depth must be uniform across the die to ensure consistency of device performance. For InP-based devices, highly selective wet etches are available and can be used to planarize the mesa etch depths, mid-process. For example, lasers with AlGaInAs quantum wells can be etched with an  $\text{H}_3\text{PO}_4:\text{H}_2\text{O}_2:\text{H}_2\text{O}$  solution, which selectively stops on the InP bottom contact layer. Since MIR laser gain material compositions depend significantly on the wavelength and active-region technology, precise fabrication steps and uniform control of the mesa etch depths must be optimized separately for each integration technique.

The following sections present an overview of MIR heterogeneously integrated lasers and SOAs on Si.

#### A. MIR Lasers on Si

The flexibility of heterogeneous integration provides the choice of which III-V gain material option is best for each wavelength and application. This is particularly important for MIR wavelengths as no single semiconductor laser technology operates throughout the entire broad 2–20  $\mu\text{m}$  regime, and the performance of each varies with wavelength. Table I shows nominal wavelength ranges for the most prominent semiconductor laser technologies which are capable of emitting light at room temperature for  $\lambda > 2 \mu\text{m}$ .

For the 2–3- $\mu\text{m}$  wavelength range, InP- and GaSb-based diode lasers [28] perform well. For wavelengths above 3  $\mu\text{m}$ , commercially available GaSb-based interband cascade lasers (ICLs) produce hundreds of mW [29], [30] with high efficiency, and InP-based quantum cascade lasers (QCLs) generate

TABLE I  
MIR SEMICONDUCTOR LASER TECHNOLOGIES

Substrate	Technology	Wavelength Range ( $\mu\text{m}$ )
InP	Type-I diode	NIR–2.4 [34]
InP	Type-II diode	$\sim 2.0$ –2.6 [35]
GaSb	Type-I diode	1.9–3.6 [36], [37]
GaSb	Interband cascade laser	2.9–7.0 [38]
InP, GaAs, InAs	Quantum cascade laser	3.0–20 [39]

Watts [31] and function out to 20  $\mu\text{m}$  [32] and in the terahertz regime [33].

#### B. 2.0- $\mu\text{m}$ Lasers and Amplifiers on Si

A variety of type-I and type-II diode lasers emit in the 2–3- $\mu\text{m}$  range, with varying performance for each technology. Integrating an InP-based type-I laser with InGaAs quantum wells is the most straightforward progression from heterogeneously integrating NIR lasers, and was the focus of the initial efforts to fabricate MIR lasers on Si. We used the SOI platform for this work, which is still suitable for wavelengths near 2.0  $\mu\text{m}$ .

The successful integration of a room-temperature continuous-wave (CW) laser with Si waveguides was only recently demonstrated in this wavelength range [40]. The III-V material used for this work (grown at nLight, Inc.) contained 4 InGaAs quantum wells for operation at 2.0- $\mu\text{m}$  wavelength. The lasers were integrated above 500-nm thick, partially etched Si waveguides.

Lasers were fabricated with designs similar to those shown in Fig. 4(a) and (b) above. The devices with a 24- $\mu\text{m}$  wide active region design included 4–6- $\mu\text{m}$  wide current channels formed by proton implantation. Fig. 6(a) shows a schematic of the active region of these devices. Unimplanted lasers with narrow 4–6- $\mu\text{m}$  wide mesas were also fabricated.

Due to the longer wavelength, the III-V material stack of these devices was slightly thicker than is typical for NIR lasers. The 2.4- $\mu\text{m}$  thick upper cladding was etched with a methane-hydrogen-argon (MHA) reactive ion etch (RIE) which was stopped with a laser monitor near the bottom of the InP layer. The field etch depth was then planarized with a selective HCl: $\text{H}_3\text{PO}_4$  (1:3) wet etch which stopped on the InGaAsP SCH layer above the active region. The remaining multiple quantum well (MQW) active region and lower cladding layers were then etched with another MHA etch step which stopped within the bottom InP contact layer.

These Fabry-Perot lasers operated in CW mode and emitted light with a wavelength of 2.01  $\mu\text{m}$ . Their maximum power was 4.2 mW and the minimum threshold current was 59 mA. More recent measurements show over 8 mW of power output from a similar device. Fig. 6(b) shows the light emission vs. drive current for this laser with a 2- $\mu\text{m}$  wide Si waveguide, a 24- $\mu\text{m}$  wide III-V mesa, and a 5- $\mu\text{m}$  wide current channel. Fig. 6(d) shows the light emission vs. drive current for a laser operating at temperatures up to 35  $^\circ\text{C}$ . A single-wavelength emission spectrum is observed from many devices, as seen in Fig. 6(c), which is attributed to multiple coupled cavities formed by reflections from the taper tips, which selected a single longitudinal mode. Finite difference time domain (FDTD) simulations suggest that

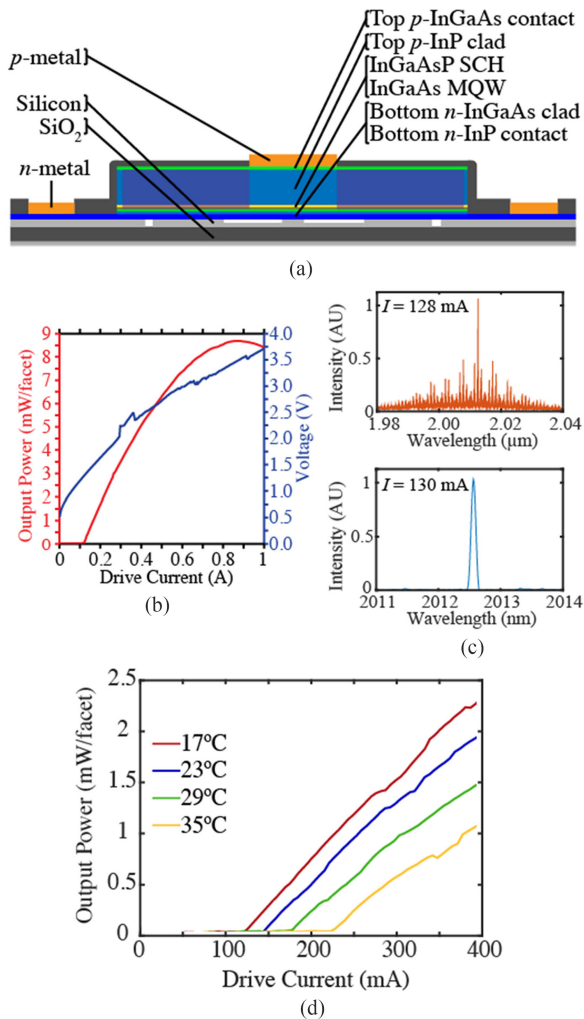


Fig. 6. (a) Cross-sectional schematic of the active region of a heterogeneously integrated  $\lambda \approx 2.0 \mu\text{m}$  laser with 4 InGaAs quantum wells above a partially etched Si waveguide. (b) CW single-sided output power versus drive current, showing a maximum of 8.7 mW at 20 °C. (c) Upper: amplified spontaneous emission spectrum of a laser operating near threshold; lower: above-threshold spectrum of a laser emitting in a single longitudinal mode with a peak wavelength of 2012.6 nm. (d) CW single-sided output power versus drive current measured at temperatures from 17 °C to 35 °C.

the reflectivity of the taper tip is near  $-18$  dB. This can be addressed by reducing the  $1.5\text{-}\mu\text{m}$  width of the active region taper tip.

Other laser structures emitting in the  $2\text{--}3\text{-}\mu\text{m}$  wavelength range have also been successfully bonded and fabricated above Si waveguides, including InP-based type-II diode Fabry-Perot [41] and distributed feedback [42] lasers operating at wavelengths near  $2.3 \mu\text{m}$ , GaSb-based lasers showing pulsed operation near  $2.38 \mu\text{m}$  from preliminary measurements [26], and an InP-based laser with InGaAs quantum wells operating in pulsed mode near  $1.9 \mu\text{m}$  [43].

The same gain structures can also be used in an SOA configuration [44], by anti-reflective coating the Si waveguide end-facets. Light from a tunable laser emitting near  $2.0\text{-}\mu\text{m}$  was injected with a lensed fiber to test the gain properties of these devices. The SOA emission was collected with another lensed

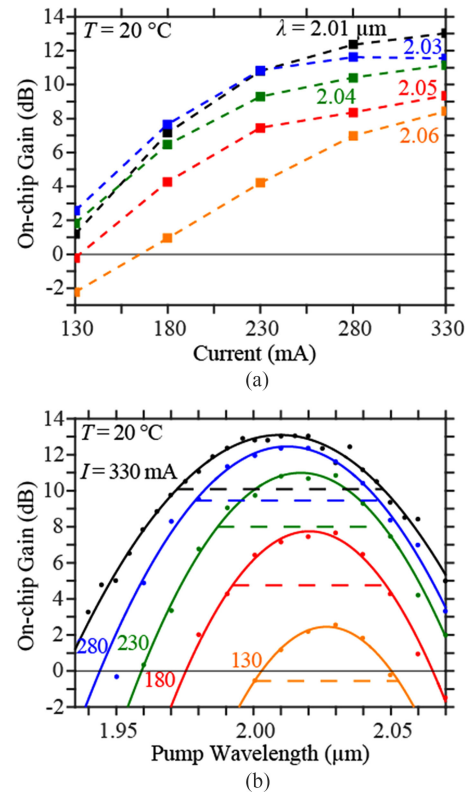


Fig. 7. On-chip gain measured at 20 °C for an integrated  $2\text{-}\mu\text{m}$  SOA (a) vs. the drive current for wavelengths from  $2.01 \mu\text{m}$  to  $2.06 \mu\text{m}$  and (b) vs. the pump wavelength for drive currents from 130 mA to 330 mA.

fiber from the opposite Si facet, and monitored with an optical spectrum analyzer.

For  $2.01\text{-}\mu\text{m}$  light, on-chip gain with a peak value of over 13-dB and 3-dB bandwidth of  $\sim 75$  nm was observed at 20 °C. These SOAs operated up to 50 °C. Fig. 7(a) shows the on-chip gain as a function of drive current for an SOA pumped with wavelengths in the range  $2.01\text{--}2.06 \mu\text{m}$ , while Fig. 7(b) shows the on-chip gain as a function of wavelength for various drive currents.

### C. $4.8\text{-}\mu\text{m}$ Lasers on Si

The first quantum cascade lasers were integrated on Si in 2016 and operated at a wavelength near  $4.8 \mu\text{m}$  [45]. Like the  $\lambda = 2.0 \mu\text{m}$  InGaAs MQW lasers, these first-generation devices were designed to form Fabry-Perot laser cavities defined by reflections from polished Si facets. To establish a broadband and versatile heterogeneous platform, the QCLs were integrated with the SONOI platform. Fully etched Si waveguides with height  $1.5 \mu\text{m}$  were constructed on top of a 400-nm thick Si<sub>3</sub>N<sub>4</sub> layer and  $3\text{-}\mu\text{m}$  thick SiO<sub>2</sub> layer on a Si substrate.

Fig. 8(a) shows a cross-sectional schematic of the active region of a heterogeneously integrated QCL. Unlike conventional heterogeneously integrated NIR lasers or the integrated  $2.0\text{-}\mu\text{m}$  wavelength lasers discussed above, proton implantation was not used for the QCLs to define a current channel. Most devices had an etched mesa design as in Fig. 4(b), while some were

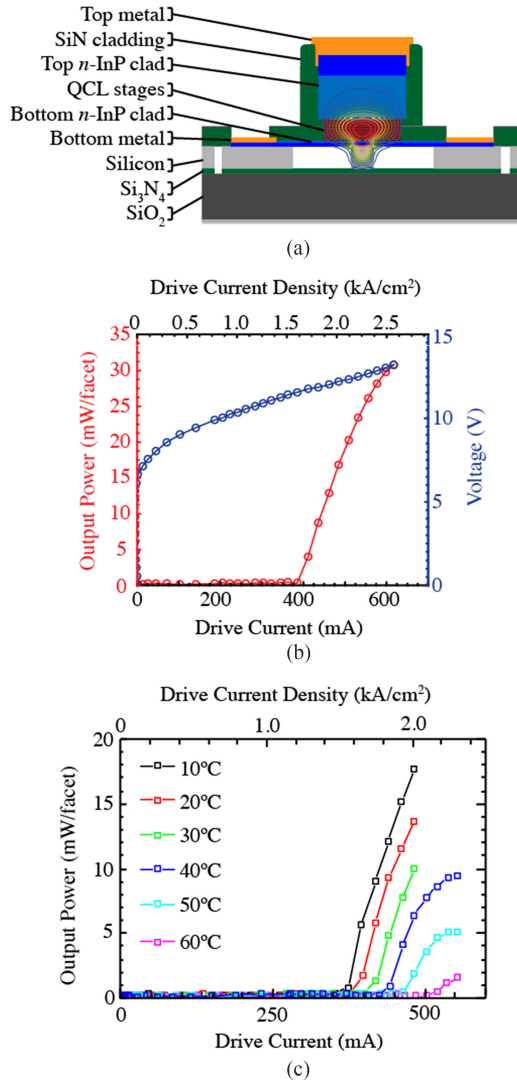


Fig. 8. (a) A cross-sectional schematic of the active region of a heterogeneously integrated 30 stage,  $\lambda \approx 4.8 \mu\text{m}$  QCL above a fully etched Si waveguide. A contour plot of the electric field component  $|E_y|$  of the fundamental TM mode is overlaid. (b) Pulsed single-sided output power and voltage vs. drive current for an integrated QCL with a  $6\text{-}\mu\text{m}$  wide III-V mesa and  $1.5\text{-}\mu\text{m}$  wide Si waveguide. A maximum of 31 mW was measured from a polished Si facet. (c) Pulsed single-sided output power versus drive current of an integrated QCL measured at temperatures from  $10^\circ\text{C}$  to  $60^\circ\text{C}$ .

fabricated with a wide active region design as in Fig. 4(c). The optical confinement in the active region ranged from  $\Gamma \approx 0.73$  to 0.76 depending on the device geometry. The hybrid III-V/Si active region was 4-mm long and the III-V tapers were either  $20 \mu\text{m}$  or  $45 \mu\text{m}$  long.

These lasers were grown on an InP substrate by metalorganic chemical vapor deposition (MOCVD) at the University of Wisconsin. The active core layers included 30 stages similar to those shown in [46]. The QCL epilayer stack designed for heterogeneous integration differed significantly from typical MQW designs. In particular, the active/injector stages composed a 1510-nm-thick region and the upper n-InP cladding and contact layers were thickened to 4050 nm to prevent optical overlap with the metal on top of the mesa. Consequently, the total QCL epi thickness of over  $5.5 \mu\text{m}$  is more than double the typical

thickness of  $\sim 2 \mu\text{m}$  for an integrated NIR diode laser [27]. To maintain the high active-region optical confinement needed for a QCL, the lower n-InP contact layer was 200-nm thick.

As a result, for heterogeneously integrated QCLs it is challenging to maintain the high etch precision required to define a tall mesa while stopping within a thin contact region, uniformly across the chip. To achieve this, an MHA RIE was used to etch through the upper n-InP layers and the active region was etched with  $\text{H}_3\text{PO}_4\text{:H}_2\text{O}_2\text{:H}_2\text{O}$  (1:5:15), which selectively stopped at the n-InP cladding below. Unfortunately this wet etch through  $\sim 1.5 \mu\text{m}$  resulted in a significant undercut of the active region, which reduced the active region taper tip length by as much as several microns on some devices. This is likely the cause of the reduced taper performance observed and discussed below.

These Fabry-Perot lasers operated in pulsed mode (250-ns wide pulses at 1-kHz repetition rate) at room temperature. Minimum threshold currents of 387 mA ( $1.6 \text{ kA}/\text{cm}^2$ ) were measured, and up to 31 mW of single-sided output power was collected from a passive SONOI waveguide. Fig. 8(b) shows the light emission vs. drive current of a QCL with a  $6\text{-}\mu\text{m}$  wide active region and  $1.5\text{-}\mu\text{m}$  wide Si waveguide. Although pulsed, this is comparable to the highest output powers reported for heterogeneously integrated lasers of any wavelength [27]. The threshold current density of  $1.6 \text{ kA}/\text{cm}^2$  is reasonably low compared to QCLs grown on native InP substrates, indicating a low internal loss within the cavity. However, the differential efficiencies in the range 150–170 mW/A are much lower than what is expected from QCLs with similar active region compositions and threshold current densities. Further analysis indicated that low taper transition efficiency and high taper reflections are most likely the cause of this performance reduction.

Fig. 8(c) shows the light emission vs. drive current for an integrated QCL, measured at temperatures in the range  $10\text{--}60^\circ\text{C}$ . The corresponding characteristic temperatures of  $T_0 = 175 \text{ K}$  and  $T_1 = 87 \text{ K}$  for threshold and slope efficiency, respectively, are comparable to those of QCLs grown on native InP substrates [46], [47].

While internal reflections that depend on polished waveguide facets are not suitable for integration within a photonic integrated circuit, wavelength-selective feedback elements, which we have integrated with lasers in the NIR [48], can be applied at longer wavelengths. In fact, Bragg reflectors for the mid-infrared are easier to define with photolithography as the grating pitch required for a first-order grating scales with wavelength.

Because the Si waveguides are processed before wafer bonding, heterogeneous integration allows the inclusion of a grating on top of the Si waveguides within the active region [49]. We consequently demonstrated distributed feedback (DFB) QCLs on Si [50] by incorporating a  $\lambda/4$ -shifted first-order grating throughout a 3-mm long active region, as illustrated in Fig. 9(a).

The threshold current densities of the DFB QCLs were typically below  $1 \text{ kA}/\text{cm}^2$ . Like the Fabry-Perot devices, these lasers also had a poor taper transmission efficiency, and initial characterization of the DFB lasers measured lower peak output powers than the previous Fabry-Perot lasers, with a maximum single-sided emission of  $\sim 11 \text{ mW}$ .

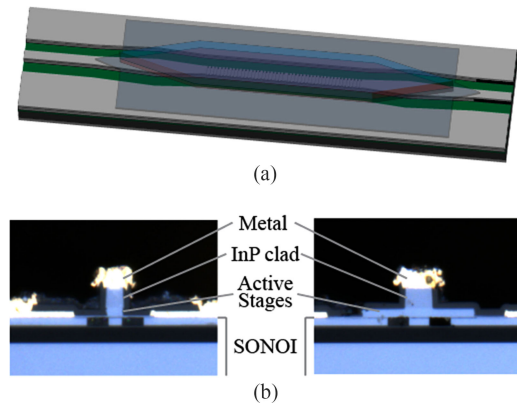


Fig. 9. (a) Three-dimensional schematic of a heterogeneously integrated DFB QCL, showing a shallow grating etched onto the surface of the Si waveguide underneath the III-V layers. (b) Polished hybrid III-V/Si facets of DFB QCLs above SONOI waveguides. Left: A 4- $\mu\text{m}$  wide, fully etched III-V mesa. Right: A 6- $\mu\text{m}$  wide upper  $n$ -InP cladding above a 24- $\mu\text{m}$  wide QCL active region.

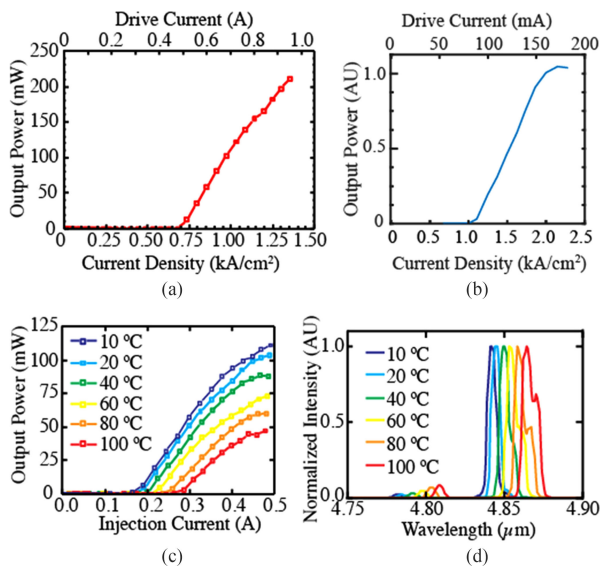


Fig. 10. (a) Pulsed light emission vs. current density from a 3-mm long DFB QCL with a 24- $\mu\text{m}$  wide active region, 6- $\mu\text{m}$  wide narrow upper cladding, and 1.5- $\mu\text{m}$  wide Si waveguide, showing a maximum peak output power of 211 mW from the polished hybrid Si/III-V facet. Current density values assume a uniform carrier distribution in the active region. (b) Pulsed light emission vs. current density from a 2-mm long DFB QCL with 4- $\mu\text{m}$  wide narrow mesa and 1.5- $\mu\text{m}$  wide Si waveguide, showing a threshold current of 80 mA. (c) Pulsed light emission vs. current density from a 3-mm long DFB QCL measured at temperatures from 10–100  $^{\circ}\text{C}$ . (d) Spectral characteristics of the same device.

The III-V taper was then polished off and the characterization repeated by measuring output from the polished hybrid III-V/Si facet, an example of which is shown in Fig. 9(b). This configuration yielded threshold current densities below  $1\text{ kA}/\text{cm}^2$ , and a minimum threshold current of 131 mA. Fig. 10(a) shows the light output vs. current density for a device with a wide active region design (Fig. 4(c)). Up to 211 mW of peak power was generated after the III-V taper was removed, and the maximum slope efficiency increased to 541 mW/A.

It is also possible to build smaller DFB lasers with lower threshold drive currents, e.g., recently-tested lasers with 2-mm

long active regions displayed similar threshold current densities of near  $1\text{ kA}/\text{cm}^2$ . Fig. 10(b) shows the light emission characteristics of a device with a threshold current of 80-mA.

Fig. 10(c) and (d) show the light output and optical spectrum vs. drive current, respectively, for an integrated DFB QCL operating at temperatures from 10  $^{\circ}\text{C}$  to 100  $^{\circ}\text{C}$ . Wavelength selectivity corresponding to the Bragg frequency of the DFB grating was observed and 22 nm of thermal tuning was achieved. However, the majority of devices did not exhibit true single-wavelength operation, most likely due to spurious reflections from the taper tip. Extracted characteristic temperatures were  $T_0 = 199\text{ K}$  and  $T_1 = 222\text{ K}$ , which are significant improvements compared to the Fabry-Perot lasers.

Although reflections and loss from the III-V tapers limited the performance of these lasers, in future processing runs it should be possible to significantly improve the efficiency of the taper transitions with improved design and fabrication. Furthermore, the thermal characteristics and relatively low threshold current densities of these lasers imply that CW lasing should be possible with improved heat dissipation. Possible solutions include the introduction of thermal shunts [51], or by bonding a thermally conductive submount to the top of the chip.

QCL gain material has been used for amplification in the past [52] and the same can be achieved on silicon to construct integrated SOAs as was achieved at 2.0  $\mu\text{m}$ . The active stages of a QCL can also be designed for operation at other wavelengths without significantly modifying the surrounding cladding layers. It is therefore possible to apply these techniques at longer or shorter wavelengths to provide laser sources throughout the MIR transmission window of Si waveguides, up to wavelengths near 7  $\mu\text{m}$ .

#### D. $>7\text{-}\mu\text{m}$ Lasers on Si

For wavelengths beyond 7  $\mu\text{m}$ , the SOI and SONOI platforms are unlikely to provide hybrid waveguides with sufficiently low loss to support lasing. However, integrated QCLs should still be practical using an alternative platform such as one based on germanium (Ge) or ( $\text{Si}_{1-x}\text{Ge}_x$ ) waveguides. Fig. 11(a) schematically illustrates two similar options for placing a Ge waveguide above a Si layer or substrate. Ge-on-Si (GOS) or Ge-on-SOI (GOSOI) waveguides can guide light from 1.9  $\mu\text{m}$  to above 10  $\mu\text{m}$  [13]. As with the SONOI platform, removing the Ge layer from the Ge-on-SOI platform will allow the fabrication of SOI waveguides that permit transmission at shorter wavelengths throughout the NIR, if the layer thicknesses are properly designed.

As with SOI and SONOI heterogeneous integration, low temperature, plasma-assisted, hydrophilic wafer bonding can be applied to bond QCL layers above GOS or GOSOI waveguides. Fig. 11(b) shows a cross-sectional schematic of a hybrid GOS/III-V active region analogous to the QCL configuration shown in Fig. 8(a). Overlaid is a contour plot of the electric field component  $|E_y|$  of the fundamental TM optical mode, which has a confinement with the active region of  $\Gamma \approx 0.77$ . Due to the high refractive index of Ge, and therefore the high effective index of GOS waveguides, a slightly narrower Ge waveguide is

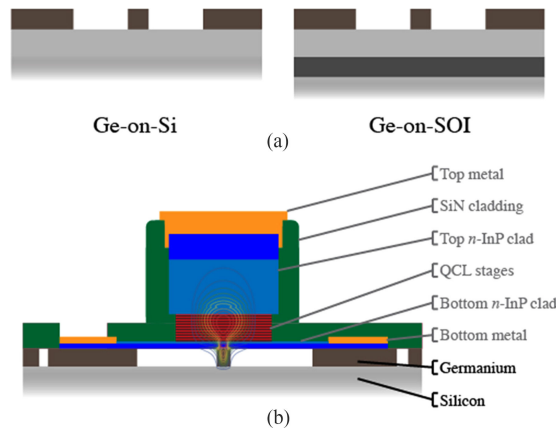


Fig. 11. (a) Cross-sectional schematic of Ge-on-Si and Ge-on-SOI waveguide platforms. (b) Cross-sectional schematic and optical mode simulation of a QCL bonded to a Ge-on-Si waveguide.

necessary to push the optical mode higher into the QCL mesa. This high refractive index may allow more efficient III-V taper transitions.

#### IV. INTEGRATED SPECTRAL BEAM COMBINING

Because heterogeneous integration allows multiple lasers operating at different wavelengths to be integrated on one chip, spectral beam combining of any of the lasers discussed in this manuscript can be used to construct a multispectral light source [23]. For densely spaced spectral channels, arrayed waveguide gratings (AWGs) have been demonstrated with low loss spanning the visible (VIS) [53] to NIR [54], and moderate loss in the MIR [55], [56].

Two methods can be used to align each laser emission wavelength to the AWG spectral combiner channel. First, the lasers can be tuned to align with the combiner channel with a feedback that maximizes the output power. The AWG can also be tuned, although that approach may be more difficult and add more loss to the AWG transmission. The second option is to design the AWG within the laser cavity. This is typically avoided since it would compromise the performance of the lasers and result in lower output power and brightness. However, with ultra-low loss AWGs having  $<0.5$  dB of loss per channel, this may nonetheless be advantageous when applied to a multispectral laser with many channels.

Fig. 12 shows the schematic for a multispectral source integrated on a single SONOI platform that combines the beams from bonded III-V lasers emitting at wavelengths ranging from  $0.4 \mu\text{m}$  to  $7 \mu\text{m}$ . In a first (intra-band) combination stage, the light produced by arrays for each band is combined into a single output waveguide by an AWG. In the second (inter-band) combination stage, light from multiple spectral bands is combined with an AWG designed to have a much coarser wavelength spacing. On a SONOI waveguide platform, the light at shorter wavelengths is generated in  $\text{Si}_3\text{N}_4$  waveguides while the light at longer wavelengths (including the MIR) is generated in Si waveguides. Then in the final combination

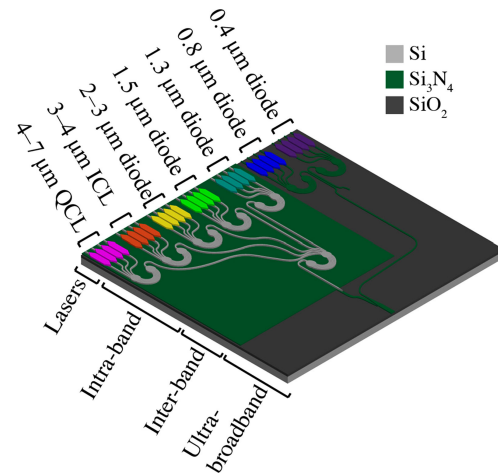


Fig. 12. Multispectral laser architecture with multiple gain materials bonded onto a Si substrate. Each laser output is spectrally combined in multiple stages to a single output waveguide.

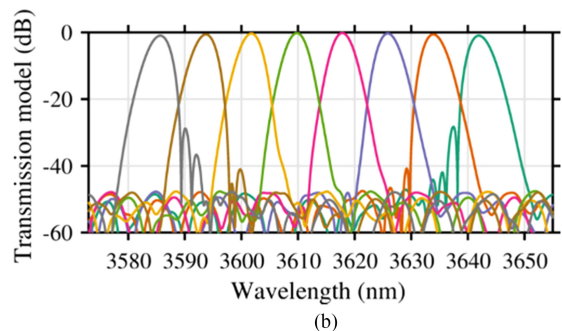
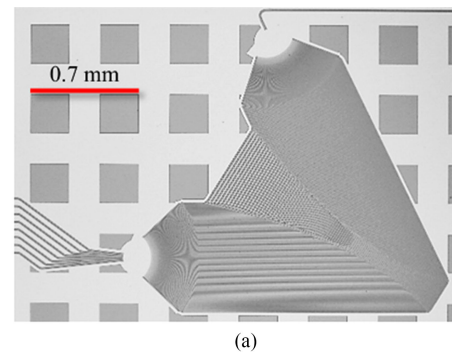


Fig. 13. (a) Micrograph of a 3.6- $\mu\text{m}$  AWG on SOI. (b) Simulated transmission spectra for this AWG.

stage, an ultra-broadband duplexer is used to combine all channels [57].

This technique is advantageous only if the loss in the spectral combiners is reduced to less than about 3 dB per channel [58]. SOI-based AWGs should provide such low loss for wavelengths up to  $\sim 3.6 \mu\text{m}$ , after which  $\text{SiO}_2$  absorption becomes detrimental. Fig. 13(a) shows a micrograph of an AWG fabricated on SOI and designed to have a center wavelength of  $\sim 3.61 \mu\text{m}$  and channel spacing of  $\sim 10$  nm. The simulated transmission spectra shown in Fig. 13(b) demonstrates low loss in the range 0.2–1.0 dB, and a crosstalk of  $-45$  dB per channel.

## V. CONCLUSION

We have overviewed Si photonic platforms and the heterogeneous integration of III-V materials with Si waveguides in the context of MIR operation. Recent lasers integrated on Si have operated at wavelengths near 2.0  $\mu\text{m}$  and 4.8  $\mu\text{m}$ .

InP-based type-I laser diodes integrated with SOI waveguides emit more than 9 mW of CW power at  $\lambda = 2.01 \mu\text{m}$  at room temperature. Integrated SOAs with the same active material provide over 13 dB of peak gain at  $\lambda = 2.01 \mu\text{m}$ .

QCLs for  $\lambda = 4.8 \mu\text{m}$  operation were integrated on the broadband SONOI waveguide platform. Fabry-Perot lasers emitted 31 mW into silicon waveguides and operated in pulsed mode up to 60 °C. DFB lasers with threshold currents as low as 80 mA and threshold current densities below 1 kA/cm<sup>2</sup> emitted >200 mW from a polished III-V/Si facet, and operated in pulsed mode up to 100 °C. Although design and fabrication modifications are necessary to improve the III-V taper transmission and to achieve CW operation, these lasers are suitable for integration into photonic integrated circuits.

By bonding QCL materials designed for emission at other wavelengths above SONOI waveguides, it should already be possible to build a mid-infrared system on silicon that combines sources and devices operating at wavelengths from 3 to 6.7  $\mu\text{m}$ .

## REFERENCES

- [1] L. S. Rothman *et al.*, “The HITRAN2012 molecular spectroscopic database,” *J. Quant. Spectrosc. Radiative Transf.*, vol. 130, pp. 4–50, Nov. 2013.
- [2] B. J. Eggleton, B. Luther-Davies, and K. Richardson, “Chalcogenide photonics,” *Nature Photon.*, vol. 5, no. 4, pp. 141–148, Feb. 2011.
- [3] Q. Xu, B. Schmidt, S. Pradhan, and M. Lipson, “Micrometre-scale silicon electro-optic modulator,” *Nature*, vol. 435, no. 7040, pp. 325–327, May 2005.
- [4] A. W.-L. Fang *et al.*, “Electrically pumped hybrid AlGaInAs-silicon evanescent laser,” *Opt. Express*, vol. 14, no. 20, pp. 9203–9210, Oct. 2006.
- [5] H.-H. Chang, Y.-H. Kuo, R. Jones, A. Barkai, and J. E. Bowers, “Integrated hybrid silicon triplexer,” *Opt. Express*, vol. 18, no. 23, pp. 23891–23899, Nov. 2010.
- [6] C. Zhang, S. Zhang, J. D. Peters, and J. E. Bowers, “8 × 8 × 40 Gbps fully integrated silicon photonic network on chip,” *Optica*, vol. 3, no. 7, pp. 785–786, Jul. 2016.
- [7] M. Muneeb *et al.*, “III-V-on-silicon integrated micro - spectrometer for the 3  $\mu\text{m}$  wavelength range,” *Opt. Express*, vol. 24, no. 9, pp. 9465–9472, May 2016.
- [8] M. Nedeljkovic *et al.*, “Mid-infrared silicon-on-insulator fourier-transform spectrometer chip,” *IEEE Photon. Technol. Lett.*, vol. 28, no. 4, pp. 528–531, Feb. 2016.
- [9] R. Wang *et al.*, “2  $\mu\text{m}$  wavelength range InP-based type-II quantum well photodiodes heterogeneously integrated on silicon photonic integrated circuits,” *Opt. Express*, vol. 23, no. 20, pp. 26834–26841, Oct. 2015.
- [10] G. Li *et al.*, “Ultralow-loss, high-density SOI optical waveguide routing for macrochip interconnects,” *Opt. Express*, vol. 20, no. 11, pp. 12035–12039, May 2012.
- [11] J. F. Bauters *et al.*, “Planar waveguides with less than 0.1 dB/m propagation loss fabricated with wafer bonding,” *Opt. Express*, vol. 19, no. 24, pp. 24090–24101, Nov. 2011.
- [12] G. Z. Mashanovich *et al.*, “Low loss silicon waveguides for the mid-infrared,” *Opt. Express*, vol. 19, no. 8, pp. 7112–7119, Mar. 2011.
- [13] R. A. Soref, S. J. Emellett, and W. R. Buchwald, “Silicon waveguided components for the long-wave infrared region,” *J. Opt. A, Pure Appl. Opt.*, vol. 8, no. 10, pp. 840–848, Aug. 2006.
- [14] A. Spott, Y. Liu, T. Baehr-Jones, R. Ilic, and M. Hochberg, “Silicon waveguides and ring resonators at 5.5  $\mu\text{m}$ ,” *Appl. Phys. Lett.*, vol. 97, no. 21, Nov. 2010, Art. no. 213501.
- [15] L. Shen *et al.*, “Mid-infrared all-optical modulation in low-loss germanium-on-silicon waveguides,” *Opt. Lett.*, vol. 40, no. 2, pp. 268–271, Jan. 2015.
- [16] Y.-C. Chang, V. Paeder, L. Hvozdar, J.-M. Hartmann, and H. P. Herzig, “Low-loss germanium strip waveguides on silicon for the mid-infrared,” *Opt. Lett.*, vol. 37, no. 14, pp. 2883–2885, Jul. 2012.
- [17] B. Troia *et al.*, “Germanium-on-silicon Vernier-effect photonic micro-cavities for the mid-infrared,” *Opt. Lett.*, vol. 41, no. 3, pp. 610–613, Feb. 2016.
- [18] W. Li *et al.*, “Germanium-on-silicon nitride waveguides for mid-infrared integrated photonics,” *Appl. Phys. Lett.*, vol. 109, no. 24, Dec. 2016, Art. no. 241101.
- [19] S. Khan, J. Chiles, J. Ma, and S. Fathpour, “Silicon-on-nitride waveguides for mid- and near-infrared integrated photonics,” *Appl. Phys. Lett.*, vol. 102, no. 12, Mar. 2013, Art. no. 121104.
- [20] J. S. Penades *et al.*, “Suspended silicon mid-infrared waveguide devices with subwavelength grating metamaterial cladding,” *Opt. Express*, vol. 24, no. 20, pp. 22908–22916, 2016.
- [21] H. Lin *et al.*, “Demonstration of high-Q mid-infrared chalcogenide glass-on-silicon resonators,” *Opt. Lett.*, vol. 38, no. 9, pp. 1470–1472, Apr. 2013.
- [22] N. Hô *et al.*, “Single-mode low-loss chalcogenide glass waveguides for the mid-infrared,” *Opt. Lett.*, vol. 31, no. 12, pp. 1860–1862, Jun. 2006.
- [23] I. Vurgaftman *et al.*, “Ultra-broadband photonic integrated circuit platform and ultra-broadband photonic integrated circuit,” U.S. Patent 9 612 398, Apr. 4, 2017.
- [24] H.-H. Chang *et al.*, “1310 nm silicon evanescent laser,” *Opt. Express*, vol. 15, no. 18, pp. 11466–11471, Sep. 2007.
- [25] D. Liang *et al.*, “High-quality 150 mm InP-to-silicon epitaxial transfer for silicon photonic integrated circuits,” *Electrochem. Solid-State Lett.*, vol. 12, no. 4, pp. H101–H104, Jan. 2009.
- [26] G. Roelkens *et al.*, “Silicon-based photonic integration beyond the telecommunication wavelength range,” *IEEE J. Sel. Topics Quantum Electron.*, vol. 20, no. 4, Jul. 2014, Art. no. 8201511.
- [27] M. L. Davenport *et al.*, “Heterogeneous Silicon/III–V semiconductor optical amplifiers,” *IEEE J. Sel. Topics Quantum Electron.*, vol. 22, no. 6, Nov. 2016, Art. no. 3100111.
- [28] S. D. Sifferman *et al.*, “Highly strained mid-infrared type-I diode lasers on GaSb,” *IEEE J. Sel. Topics Quantum Electron.*, vol. 21, no. 6, Nov. 2015, Art. no. 1502410.
- [29] I. Vurgaftman *et al.*, “Interband cascade lasers,” *J. Phys. D, Appl. Phys.*, vol. 48, no. 12, Mar. 2015, Art. no. 123001.
- [30] C. L. Canedy *et al.*, “Pulsed and CW performance of 7-stage interband cascade lasers,” *Opt. Express*, vol. 22, no. 7, pp. 7702–7710, Apr. 2014.
- [31] Y. Bai, N. Bandyopadhyay, S. Tsao, S. Slivken, and M. Razeghi, “Room temperature quantum cascade lasers with 27% wall plug efficiency,” *Appl. Phys. Lett.*, vol. 98, no. 18, pp. 181102–181104, May 2011.
- [32] M. Bahriz, G. Lollia, A. N. Baranov, and R. Teissier, “High temperature operation of far infrared ( $\lambda \approx 20 \mu\text{m}$ ) InAs/AlSb quantum cascade lasers with dielectric waveguide,” *Opt. Express*, vol. 23, no. 2, pp. 1523–1528, Jan. 2015.
- [33] B. S. Williams, “Terahertz quantum-cascade lasers,” *Nature Photon.*, vol. 1, no. 9, pp. 517–525, Sep. 2007.
- [34] Y. Gu *et al.*, “2.4  $\mu\text{m}$  InP-based antimony-free triangular quantum well lasers in continuous-wave operation above room temperature,” *Appl. Phys. Express*, vol. 7, no. 3, Feb. 2014, Art. no. 032701.
- [35] S. Sprengel *et al.*, “InP-based type-II quantum-well lasers and LEDs,” *IEEE J. Sel. Topics Quantum Electron.*, vol. 19, no. 4, Jul. 2013, Art. no. 1900909.
- [36] H. K. Choi, G. W. Turner, and S. J. Eglash, “High-power GaInAsSb-AlGaAsSb Multiple-Quantum-Well diode lasers emitting at 1.9  $\mu\text{m}$ ,” *IEEE Photon. Technol. Lett.*, vol. 6, no. 1, pp. 7–9, Jan. 1994.
- [37] K. Vizbaras and M. C. Amann, “3.6  $\mu\text{m}$  GaSb-based type-I lasers with quaternary barriers, operating at room temperature,” *Electron. Lett.*, vol. 47, no. 17, pp. 980–981, Aug. 2011.
- [38] J. Scheuermann *et al.*, “Single-mode interband cascade laser sources for mid-infrared spectroscopic applications,” in *Proc. SPIE Commercial + Scientific Sensing Imaging*, 2016, vol. 9855, Paper 98550G–6.
- [39] Y. Yao, A. J. Hoffman, and C. F. Gmachl, “Mid-infrared quantum cascade lasers,” *Nature Photon.*, vol. 6, no. 7, pp. 432–439, Jun. 2012.
- [40] A. Spott *et al.*, “Heterogeneously integrated 2.0  $\mu\text{m}$  CW hybrid silicon lasers at room temperature,” *Opt. Lett.*, vol. 40, no. 7, pp. 1480–1483, Apr. 2015.
- [41] R. Wang *et al.*, “2.3  $\mu\text{m}$  range InP-based type-II quantum well Fabry-Perot lasers heterogeneously integrated on a silicon photonic integrated circuit,” *Opt. Express*, vol. 24, no. 18, pp. 21081–21089, Sep. 2016.

- [42] R. Wang *et al.*, "Heterogeneously integrated III-V-on-silicon 2.3x  $\mu\text{m}$  distributed feedback lasers based on a type-II active region," *Appl. Phys. Lett.*, vol. 109, no. 22, Dec. 2016, Art. no. 221111.
- [43] P. Dong *et al.*, "1.9  $\mu\text{m}$  hybrid silicon/III-V semiconductor laser," *Electron. Lett.*, vol. 49, no. 10, pp. 664–666, May 2013.
- [44] N. Volet *et al.*, "Semiconductor optical amplifiers at 2.0- $\mu\text{m}$  wavelength on silicon," *Laser Photon. Rev.*, vol. 11, no. 2, Feb. 2017, Art. no. 1600165.
- [45] A. Spott *et al.*, "Quantum cascade laser on silicon," *Optica*, vol. 3, no. 5, pp. 545–551, May 2016.
- [46] A. Evans *et al.*, "Buried heterostructure quantum cascade lasers with high continuous-wave wall plug efficiency," *Appl. Phys. Lett.*, vol. 91, no. 7, Aug. 2007, Art. no. 071101.
- [47] J. S. Yu *et al.*, "High-power, room-temperature, and continuous-wave operation of distributed-feedback quantum-cascade lasers at  $\lambda \sim 4.8 \mu\text{m}$ ," *Appl. Phys. Lett.*, vol. 87, no. 4, Jul. 2005, Art. no. 041104.
- [48] T. Komljenovic *et al.*, "Widely tunable narrow-linewidth monolithically integrated external-cavity semiconductor lasers," *IEEE J. Sel. Topics Quantum Electron.*, vol. 21, no. 6, Nov. 2015, Art. no. 1501909.
- [49] C. Zhang *et al.*, "Low threshold and high speed short cavity distributed feedback hybrid silicon lasers," *Opt. Express*, vol. 22, no. 9, pp. 10202–10209, May 2014.
- [50] A. Spott *et al.*, "Heterogeneously integrated distributed feedback quantum cascade lasers on silicon," *Photonics*, vol. 3, no. 2, p. 35, Jun. 2016.
- [51] M. N. Sysak *et al.*, "Hybrid silicon laser technology: A thermal perspective," *IEEE J. Sel. Topics Quantum Electron.*, vol. 17, no. 6, pp. 1490–1498, Nov. 2011.
- [52] S. Menzel *et al.*, "Quantum cascade laser master-oscillator power-amplifier with 1.5 W output power at 300 K," *Opt. Express*, vol. 19, no. 17, pp. 16229–16235, Aug. 2011.
- [53] E. J. Stanton, A. Spott, M. L. Davenport, N. Volet, and J. E. Bowers, "Low-loss arrayed waveguide grating at 760 nm," *Opt. Lett.*, vol. 41, no. 8, pp. 1785–1788, Apr. 2016.
- [54] J. F. Bauters, J. R. Adleman, M. J. R. Heck, and J. E. Bowers, "Design and characterization of arrayed waveguide gratings using ultra-low loss Si<sub>3</sub>N<sub>4</sub> waveguides," *Appl. Phys. A*, vol. 116, no. 2, pp. 427–432, Jun. 2014.
- [55] M. Muneeb *et al.*, "Demonstration of silicon-on-insulator mid-infrared spectrometers operating at 3.8  $\mu\text{m}$ ," *Opt. Express*, vol. 21, no. 10, pp. 11659–11669, May 2013.
- [56] A. Malik *et al.*, "Germanium-on-silicon mid-infrared arrayed waveguide grating multiplexers," *IEEE Photon. Technol. Lett.*, vol. 25, no. 18, pp. 1805–1808, Sep. 2013.
- [57] E. J. Stanton, M. J. R. Heck, J. Bovington, A. Spott, and J. E. Bowers, "Multi-octave spectral beam combiner on ultra-broadband photonic integrated circuit platform," *Opt. Express*, vol. 23, no. 9, pp. 11272–11283, May 2015.
- [58] T. Y. Fan, "Laser beam combining for high-power, high-radiance sources," *IEEE J. Sel. Topics Quantum Electron.*, vol. 11, no. 3, pp. 567–577, May 2005.



**Alexander Spott** (S'10–GS'17) received the B.S. degree in physics in 2011 from the University of Washington, Seattle, WA, USA, and the M.S. degree in electrical and computer engineering in 2015 from the University of California, Santa Barbara, CA, USA, where he is currently working toward the Ph.D. degree.

His research has focused on mid-infrared optoelectronics and silicon photonic integration. He has authored or coauthored more than 25 journal and conference papers which have been cited over 250 times.

He received a National Science Foundation Graduate Research Fellowship in 2012.



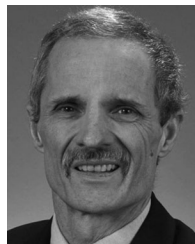
**Eric J. Stanton** (S'08–GS'13) received the B.S. degree in electrical engineering in 2012 from California Polytechnic State University San Luis Obispo, San Luis Obispo, CA, USA, and the M.S. degree in electrical and computer engineering in 2014 from the University of California, Santa Barbara, CA, USA, where he is currently working toward the Ph.D. degree with emphasis in photonics, focusing on devices for multi-octave spectral combining of heterogeneously integrated lasers on silicon.



**Nicolas Volet** received the Ph.D. degree in physics from École Polytechnique Fédérale de Lausanne, Lausanne, Switzerland, in 2014. He developed a new technology to control the optical mode of vertical-cavity surface-emitting lasers operating in the O- and in the C-bands. He also contributed to the understanding of the polarization properties of these devices, both theoretically and experimentally. He is currently a Postdoctoral Researcher at the University of California, Santa Barbara, CA, USA, where he works on nonlinear optics and photonics devices heterogeneously integrated on silicon. Dr. Volet received a one-year scholarship (2006–2007) at Carnegie Mellon University, Pittsburgh, and during 2008–2009, he worked on solar cells based on quantum confinement at the University of Houston. He received research fellowships from the Swiss National Science Foundation in 2014 and 2016.



**Jonathan D. Peters** has more than 13 years of process experience in the MEMS and semiconductor field. He was with Applied Magnetics Corporation in Santa Barbara as an Operator, Process Inspector, and Plate And Etch Technician for five years before moving to Solus Micro Technologies/NP Photonics in Westlake Village as a Process Engineer for four years. He moved back to Santa Barbara to work at Innovative Micro Technology as a Process Engineer and an R&D Engineer for four years before coming to work for the Bowers Group at the University of California, Santa Barbara, in 2008.



**Jerry R. Meyer** (F'04) received the Ph.D. degree in physics from Brown University, Providence, RI, USA, in 1977. Since then he has carried out basic and applied research at the Naval Research Laboratory, Washington, DC, USA, where he is the Navy Senior Scientist for Quantum Electronics (ST). He has coauthored more than 370 refereed journal articles which have been cited more than 20 000 times (H-Index 58), 16 book chapters, 33 patents (7 licensed), and more than 160 invited conference presentations. His research has focused on semiconductor optoelectronic materials and devices such as new classes of semiconductor lasers and detectors for the infrared. He is a Fellow of the OSA, APS, IOP, and SPIE. He received the Presidential Rank Award, ONR's Captain Robert Dexter Conrad Award for Scientific Achievement (2015), NRL's E. O. Hulbert Annual Science Award (2012), and the IEEE Photonics Society Engineering Achievement Award (2012).



**John E. Bowers** (F'94) received the M.S. and Ph.D. degrees from Stanford University, Stanford, CA, USA. He holds the Fred Kavli Chair in Nanotechnology, and is the Director of the Institute for Energy Efficiency and a Professor in the Departments of Materials and Electrical and Computer Engineering at the University of California, Santa Barbara (UCSB). He is a Cofounder of Aurrion, Aerius Photonics and Calient Networks. He was with AT&T Bell Laboratories and Honeywell before joining UCSB. He has published eight book chapters, 700 journal papers, 900 conference papers, and has received 64 patents. He is a member of the National Academy of Engineering and the National Academy of Inventors. He is a Fellow of the OSA and the American Physical Society, and received the IEEE Photonics Award, the OSA Tyndal Award, the OSA Holonyak Prize, the IEEE LEOS William Streifer Award, and the South Coast Business and Technology Entrepreneur of the Year Award. He and coworkers received the EE Times Annual Creativity in Electronics Award for Most Promising Technology for the hybrid silicon laser in 2007.